PHILOSOPHICAL TRANSACTIONS A

rsta.royalsocietypublishing.org

Research

Cite this article: Wang N, Kocher G, Provatas N. 2018 A phase-field-crystal alloy model for late-stage solidification studies involving the interaction of solid, liquid and gas phases. *Phil. Trans. R. Soc. A* **376**: 20170212.
http://dx.doi.org/10.1098/rsta.2017.0212

Accepted: 4 October 2017

One contribution of 16 to a theme issue 'From atomistic interfaces to dendritic patterns'.

Subject Areas:
mesoscopics, thermodynamics, statistical physics, solid state physics

Keywords:
phase field, solidification, defects, shrinkage

Author for correspondence:
Nikolas Provatas
e-mail: provatas@physics.mcgill.ca

A phase-field-crystal alloy model for late-stage solidification studies involving the interaction of solid, liquid and gas phases

Nan Wang, Gabriel Kocher and Nikolas Provatas

Department of Physics, McGill University, Montreal, Québec, Canada

NW, 0000-0002-1012-0992

We present a multiphase binary alloy phase-field-crystal model. By introducing density difference between solid and liquid into a previous alloy model, this new fusion leads to a practical tool that can be used to investigate formation of defects in late-stage alloy solidification. It is shown that this model can qualitatively capture the liquid pressure drop due to solidification shrinkage in confined geometry. With an inherited gas phase from a previous multiphase model, cavitation of liquid from shrinkage-induced pressure is also included in this framework. As a unique model that has both solute concentration and pressure-induced liquid cavitation, it also captures a modified Scheil–Gulliver-type segregation behaviour due to cavitation. Simulation of inter-dendritic channel solidification using this model demonstrates a strong cooling rate dependence of the resulting microstructure.

This article is part of the theme issue 'From atomistic interfaces to dendritic patterns'.

1. Introduction

Phase-field-crystal (PFC) methodology has been gaining popularity due to its unique capability in modelling crystalline materials [1–4]. In the past decade, it has been used to investigate the physical mechanisms of many interesting problems such as solid-state structural transformation [5–7], crystal and gas phase nucleation [8, 9], dislocation dynamics [10], interface instability [11, 12] and electromigration [13]. The methodology has also been extended to binary and multicomponent alloys [7], multiple crystal structures [5] and multiphase systems [9].

THE ROYAL SOCIETY PUBLISHING

This work further extends the PFC phenomenology by introducing a binary PFC model that supports a low-density vapour phase. This is done by fusing features of two previous PFC models, the binary PFC of Elder *et al.* [2] and the PFC model of pure materials of Kocher *et al.* [9]. The introduction of a vapour phase into solidification modelling is relevant to processes ranging from solidification shrinkage and cavitation to CVD growth. As such, the model formulated here is demonstrated in the context of phenomena relevant to late-stage solidification.

Solidification of alloy has been a topic of both theoretical and practical importance for many years [14,15]. Computational modelling of crystallization microstructure evolution has led to significant progress in our understanding of solidification [16,17]. At low solid volume fraction, classic solidification theories have been developed to predict the properties of dendritic patterns, whose fundamental length scale is tied to the Mullins–Sekerka instability wavelength [14], which is on the order of micrometres. At very high solid volume fraction (99% and above), the size of interdendritic/intergranular liquid films are narrowed down to the order of nanometers, which is comparable to the solid–liquid interface width. This occurs during the late stage of solidification, where liquid transport is gradually shut down by increasing solid confinement. This regime is a transition from a diffusion controlled process at low solid fraction to a surface energy-controlled process at very high solid fraction. Theories based on interface disjoining potentials have been developed recently to explain grain coalescence and bridging of grains in the last stages of solidification [18–20]. Some of these are based on the PFC methodology, which operates at 10–100 nm, the length scales required to investigate the late-stage solidification process.

Another important behaviour of late stage solidification that has long been known is associated with the formation of defects and second-phase particles [15]. Gas-phase defects, such as microporosity and hot tears, in particular, form at this stage and are imprinted into the final solidified microstructure. However, our knowledge on late-stage solidification of low concentration alloys is still very limited despite its strong impact on final material properties [18].

In the classic picture of late-stage solidification, a partially solidified region with a small liquid-volume fraction is called mushy zone and is heuristically considered a 'semi-solid' [15]. Many experimental and theoretical studies have been dedicated to understand materials' behaviour in the mushy zone [21–26]. As there is typically a density difference between the solid and the liquid, solidification in this confined environment has been known to generate local pressure drop due to shrinkage of the solid caused by density change. It has been shown in experiments that the pressure induced from solidification shrinkage may lead to porosity formation, hot tearing failure, deformation of the dendritic network and even recrystallization in solidified structure [27–30]. Niyama's criterion was developed to explain the formation of gas porosity [31] in narrow liquid channels. Rappaz, Drezet and Gremaud (RDG) developed a two-phase theory that takes into account both elastic and plastic deformation of the solid confining the narrow liquid channels that form hot tears [32]. The nucleation of the gas phase (or cavitation) in these continuum-based models is typically determined by setting up a pressure threshold which can be obtained from atomic-level models [33,34].

Another important phenomenon at the late stages of solidification is the precipitation of non-equilibrium or second phases [35]. Continuous enrichment of the confined liquid melts due to solute rejection at the solidification front (commonly known as microsegregation) leads to the formation of small secondary solid phases below the eutectic point [36–38]. Materials' strength can be strongly affected by the size and distribution of those small particles [39,40]. Based on local solute partitioning, the Scheil–Gulliver (SG) equation has been widely used to explain the solute enrichment in eutectic liquid at the late stage.

A comprehensive microscopic continuum model for late-stage solidification is presently lacking because it requires a model that is capable of capturing solute segregation, solidification shrinkage, gas-phase nucleation, and elastic and potential plastic deformation in the solid under confinement [41]. Existing PFC models in the literature have been shown to contain some of these physics separately, but none within a single framework. The focus of this work will be to extend the original PFC phenomenology to consistently capture the aforementioned physics of late-stage solidification in a single theory.

The paper is structured in four sections. Section II presents the model formulation, and some of its alloy and multiphase equilibrium properties are demonstrated. Dynamical evolution for a multiphase alloy system are then discussed. In §3, the model is shown to reproduce typical shrinkage-induced pressure drop in the liquid near the solidification front. A modification of the late-stage SG-type microsegregation behaviour is then predicted due to gas-phase nucleation. Following this, solidification of interdendritic liquid at different cooling rates is also discussed, and a new effect of a gas-induced mechanism for precipitation is presented. The last section concludes the work and discusses future outlook on the use of the model.

2. Model formulation

This section begins by introducing a minimal PFC model that can be used to study cavitation in alloy solidification; we begin from previous alloy models [2,7] and a recently developed gas-phase model [9]. The parameters in this new model can be traced back to either of the aforementioned alloy models or the gas-phase model. Using basic thermodynamics, classic binary alloy behaviour is demonstrated in the model. Transitions from high-density phases (α, β solid and liquid) to a low-density gas phase, and corresponding density change during solidification, are then demonstrated. Dynamics for the microscopic PFC density and concentration are proposed, with the dynamics of the latter field taking into account inhomogeneity in the average density.

(a) Free energy functional

The dimensionless free energy functional is written in terms of a dimensionless PFC density field $n(\mathbf{r}) = (\rho - \bar{\rho})/\bar{\rho}$, where $\bar{\rho}$ is the reference fluid density around which the theory is expanded, and a concentration filed $c(\mathbf{r})$ (as in previous alloy models [2,7]). Its form is the sum of an ideal contribution F_{ideal}, the pair correlation contribution F_{pair} and the multi-point correlation contribution F_{MP}, i.e.

$$F_{\text{PFC}} = F_{\text{ideal}} + F_{\text{pair}} + F_{\text{MP}}. \tag{2.1}$$

The ideal part of the free energy is expanded as

$$F_{\text{ideal}} = \int \left[\epsilon \frac{n(\mathbf{r})^2}{2} - W_1 \frac{n(\mathbf{r})^3}{6} + W_2 \frac{n(\mathbf{r})^4}{12} \right] \mathrm{d}\mathbf{r}, \tag{2.2}$$

where ϵ, W_1 and W_2 are constants of the model. Here, the spatial coordinate is scaled by a reference solid-phase lattice constant. The pair correlations term has three parts

$$F_{\text{pair}} = F_{\text{nn}} + F_{\text{nc}} + F_{\text{cc}}, \tag{2.3}$$

where F_{nn} denotes density correlations, F_{cc} correlations in concentration and F_{nc} density–concentration correlations. The term F_{nn} is written as

$$F_{\text{nn}} = \frac{1}{2} \int n(\mathbf{r}_1) \left\{ \int [\xi(c) C^{\text{AA}}(\mathbf{r}_1 - \mathbf{r}_2) + \xi(1-c) C^{\text{BB}}(\mathbf{r}_1 - \mathbf{r}_2)] n(\mathbf{r}_2)\, \mathrm{d}\mathbf{r}_2 \right\} \mathrm{d}\mathbf{r}_1. \tag{2.4}$$

For the density pair correlation functions in the above equation, we consider here single peak approximations, i.e. $C^{\text{AA}} = B_{x1}(q_1^2 + \nabla^2)^2$ and $C^{\text{BB}} = B_{x2}(q_2^2 + \nabla^2)^2$, where q_1 and q_2 set the first peak positions of the crystal structures corresponding to the limits $c = 0$ and and $c = 1$, respectively, in reciprocal space. The function ξ is smooth and interpolates crystal structure between $c = 0$ and $c = 1$, as in Greenwood *et al.* [7]. The solid-phase lattice constant a is given by $a = 4\pi/(\sqrt{3}q_1)$. The F_{nc} term is a modification of a term in Koher *et al.* [9] given by

$$F_{\text{nc}} = \int \zeta(c(\mathbf{r}_1)) n(\mathbf{r}_1) \left[\int \chi_{\text{c}}(\mathbf{r}_1 - \mathbf{r}_2) \zeta(c(\mathbf{r}_2)) n(\mathbf{r}_2)\, \mathrm{d}\mathbf{r}_2 \right] \mathrm{d}\mathbf{r}_1, \tag{2.5}$$

where $\zeta(c)$ is a function specified below and the density–concentration pair correlation is approximated by $\chi_{\text{c}}(\mathbf{k}) = \mathrm{e}^{-\mathbf{k}^2/2\lambda_{\text{c}}}$ in reciprocal space, where λ_{c} is a constant. The F_{cc} term follows

the standard form

$$F_{\mathrm{cc}} = \int \alpha |\nabla c|^2 \, \mathrm{d}\mathbf{r}, \tag{2.6}$$

where α is a constant. The contribution from multi-point correlations follows Kocher *et al.* [9],

$$F_{\mathrm{MP}} = \sum_{m=3}^{4} \frac{1}{m} \int \mathrm{d}\mathbf{r}_1 \ldots \mathrm{d}\mathbf{r}_m \chi_m(\mathbf{r}_1, \ldots, \mathbf{r}_m) n(\mathbf{r}_1) \ldots n(\mathbf{r}_m), \tag{2.7}$$

where $\chi_3 = (a_1\epsilon + b_1)\chi(\mathbf{r}_1 - \mathbf{r}_2)\chi(\mathbf{r}_1 - \mathbf{r}_3)$ and $\chi_4 = c_1\chi(\mathbf{r}_1 - \mathbf{r}_2)\chi(\mathbf{r}_1 - \mathbf{r}_3)\chi(\mathbf{r}_1 - \mathbf{r}_4)$, with $\chi(\mathbf{k}) = \mathrm{e}^{-\mathbf{k}^2/2\lambda}$ in reciprocal space. The parameters λ, a_1, b_1 and c_1 are constants. Assuming the concentration field c changes slowly on the scale of the atomically varying density $n(\mathbf{r})$, equation (2.5) is approximated by replacing $c(\mathbf{r}_2)$ with $c(\mathbf{r}_1)$ and choosing

$$|\zeta(c)|^2 = \frac{u_1}{2}(c - c_0)^2 + \frac{v_1}{4}(c - c_0)^4, \tag{2.8}$$

where u_1, v_1 are constants and c_0 is a reference concentration.

(b) Thermodynamic properties

The terms comprising equation (2.1) are parametrized by the set $\{\epsilon, W_1, W_2, B_{x1}, B_{x2}, q_1, q_2, u_1, v_1, c_0, \lambda_c, \lambda, a_1, b_1, c_1\}$. These constants can be determined by matching the model's behaviour to the thermodynamic and material properties of an experimental system. This can be done, for instance, by following an analogous approach to that of Asadi & Zaeem [42], which matches the parameters of a PFC model of a pure material to the elastic constants, solid–liquid coexistence densities, density expansion and compressibility of Fe. For an alloy system, we require the additional properties, including the determination of density expansion and coexistence densities associated with the liquid–vapour and solid–vapour phase changes, all of which vary with c. These can be uniquely determined by exploiting the larger parameter set associated with the present model. This endeavour requires considerable effort to implement and will be the topic of a future study and publication. In this work, we will restrict ourselves to selecting parameters in ranges where the desired physical properties of a 2-solid–liquid–vapour alloy system are qualitatively demonstrated.

We begin by choosing the model parameters to reproduce the thermodynamic features of a typical binary alloy system at different values of the temperature parameter ϵ. The model parameters used in this work are shown in the caption of figure 1. The free energy plot in figure 1*a* shows two separate solid–liquid coexistence regions as a function of concentration. With the temperature parameter ϵ sitting above the eutectic point, there is no overlap between the coexistence regions along the concentration axis. At a lower temperature, the two coexistence regions start to merge, as shown in figure 1*b*. Below the eutectic point, there is a large coexistence region between alpha and beta solids, as shown in figure 1*c*.

A crucial physical mechanism that has long been accepted to be responsible for many late-stage solidification phenomena is the change of density associated with solid–liquid phase transition. As expected, the current model parameters are chosen such that both α and β solids have a higher density than the liquid phase, for a given concentration. This behaviour of the model is shown in figure 2.

To study cavitation due to solidification shrinkage, one of the fundamental causes of subsequent cracking, the model's parameter set must be in a range that allows the model to simultaneously capture both solid–vapour and liquid–vapour phase transitions in an alloy system. The vapour phase is obtained by introducing a low-density minimum in the uniform branch of the PFC free energy using the technique in [9]. As the model is intended to be used for solidification, and it is known that nucleation of the gas phase during solidification is related to shrinkage-induced pressure drop in the liquid (demonstrated in a later section), the uniform branch of the free energy must have a liquid–vapour coexistence region with dropping temperature parameter ϵ. This property is shown in figure 3.

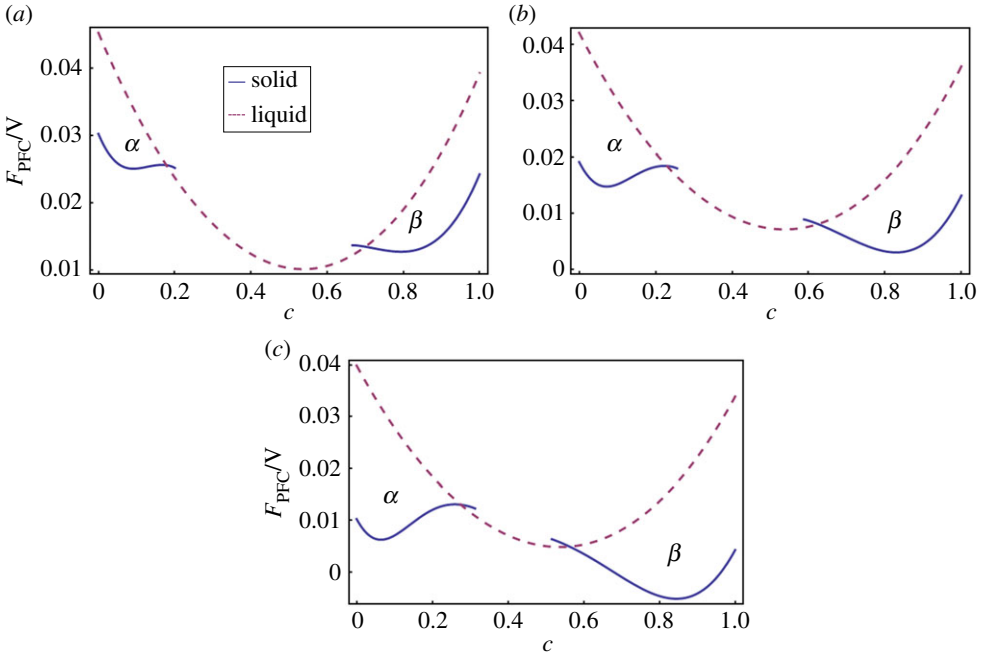

Figure 1. Thermodynamic properties of the PFC model mimicking a binary alloy system. Here, c is the mean concentration. α and β refer to the two solids, respectively. (*a*) $\epsilon = 0.26$ (above the eutectic point), (*b*) $\epsilon = 0.237$ (near the eutectic point) and (*c*) $\epsilon = 0.22$ (below the eutectic point). Model parameters used in this work are $W_1 = 1.3$, $W_2 = 0.6$, $\alpha = 8.0$, $B_{x1} = 0.3$, $B_{x2} = 0.9$, $q_1 = \sqrt{2}$, $q_2 = 1$, $u_1 = 6.0$, $v_1 = 3.0$, $c_0 = 0.5$, $a_1 = 43$, $b_1 = -30$, $c_1 = 90$, $\lambda = \lambda_c = 0.04$. Free energies are evaluated using equation (2.1) with mean density $n_0 = 0.2$. (Online version in colour.)

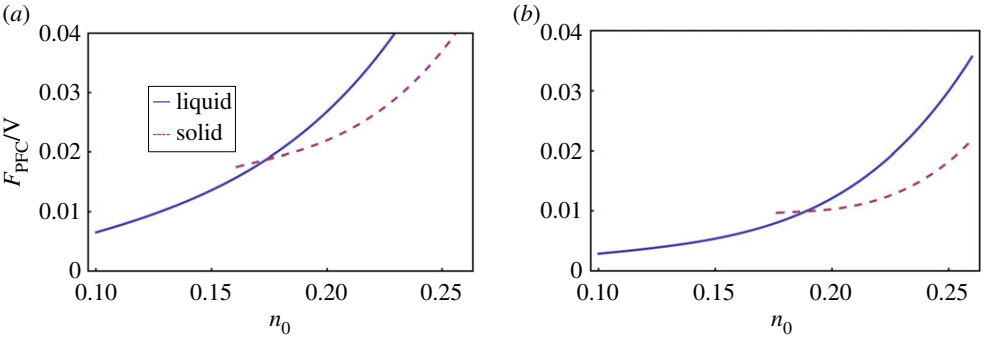

Figure 2. Density shift in solid–liquid phase transition in this model. (*a*) $\epsilon = 0.25$, $c = 0.15$ (in α-liquid coexistence region). (*b*) $\epsilon = 0.25$, $c = 0.75$ (in β-liquid coexistence region). Other model parameters are given in figure 1. (Online version in colour.)

While the shrinkage-induced pressure in solidification may lead to liquid cavitation as described above, it can also lead to plastic deformation, voids and cracks in the solid state. This is particularly true in rapid solidification. Therefore, it is necessary to correctly model the thermodynamics that capture the coexistence of α and β solids with a low-density vapour phase below the eutectic point. This physical property of the model is shown in figure 4.

The present alloy PFC model is specifically constructed to augment the physical properties of the original alloy model of Elder *et al.* [2] with the demonstrated vapour-phase thermodynamics above. The properties incorporated into the alloy PFC model allow for a vapour phase that

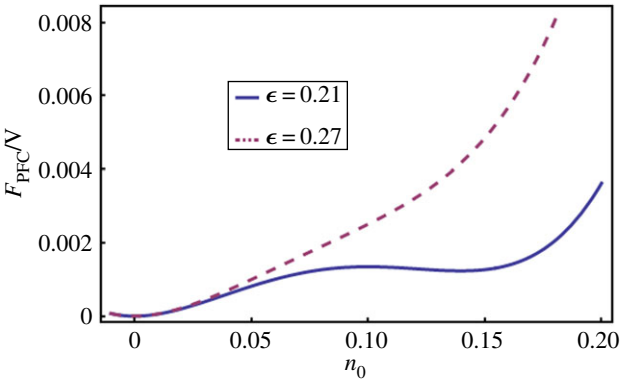

Figure 3. Free energy of the uniform branch of the PFC model in equation (2.1) versus mean density n_0, shown at two temperature parameters. At low temperature, the uniform phase gives rise to a high-density well that is the liquid state, while the low-density well is in the vapour state. The average concentration is set to $c = 0.5$. Other model parameters are given in figure 1. (Online version in colour.)

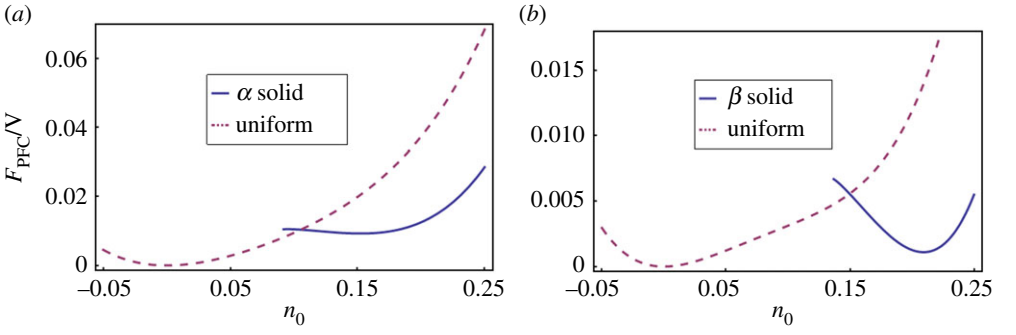

Figure 4. Coexistence of the low-density uniform phase (vapour) with α solid (*a*) and β solid (*b*). Here, n_0 is the mean density. Temperature parameter is set to $\epsilon = 0.23$ (below the eutectic point). The average concentration for frame (*a*) is set to $c = 0.03$, and $c = 0.75$ for frame (*b*) β solid. Other model parameters are given in figure 1. (Online version in colour.)

can coexist with both liquid and solids, and thus can serve to study the mechanism of cavitation/voiding that is induced by solidification shrinkage. The parameter range in which the above thermodynamic behaviour is exhibited was observed to be robust enough to be able to also capture other interesting phenomena.

(c) Evolution equations

Dynamical evolution of PFC density n follows conserved variational dynamics given by

$$\frac{\partial n}{\partial t} = \nabla \cdot \left(M_n \nabla \frac{\delta F}{\delta n} \right) + \eta, \tag{2.9}$$

while the concentration c evolves according to

$$(1 + \bar{n}) \frac{\partial c}{\partial t} = \nabla \cdot \left[(1 + \bar{n}) M_c \nabla \frac{\delta F}{\delta c} \right], \tag{2.10}$$

The corresponding mobilities M_n and M_c control the diffusive timescale of the c and n fields, respectively. The variable $\bar{n}(r) = \int n(r')\chi(r - r')\,\mathrm{d}r'$ is the locally averaged spatial density, and the stochastic noise η satisfies the fluctuation–dissipation theorem $\langle \eta(\mathbf{r}, t), \eta(\mathbf{r}', t') \rangle =$

$-2(M_n/\bar{\rho}a^d)\nabla^2\delta(\mathbf{r}-\mathbf{r}')\delta(t-t')$, where $\bar{\rho}$ is the reference density about which the PFC model is expanded. As c is not, in general, a conserved field as in previous PFC models, equation (2.10) approximates c dynamics by weighing changes in solute concentration with the local average density. It is clear that this generalized concentration dynamics for spatially inhomogeneous $\bar{n}$ is reduced to the classic concentration dynamics when $\bar{n}$ is assumed to be constant in the system as in previous PFC literature. It has been shown that nucleation-related critical fluctuations are essentially on the interface length scale, therefore, we only included a noise term in the atomically resolved PFC order parameter field n and ignored fluctuations in the slow varying concentration field c.

Numerical implementation of the dynamics in equation (2.9) and (2.10) is based on Fourier space semi-implicit algorithm. Details of the algorithm is given in appendix A.

3. Demonstrations and predictions of the model

This section begins by benchmarking our PFC model against a well-known phenomenon associated with the late-stage solidification processes. Namely, we show that the model qualitatively captures the pressure drop induced by solidification shrinkage inside an inter-dendritic liquid channel. Then, our model is used to predict how the SG microsegregation relation is modified in the presence of a gas phase. Finally, we examine cooling-rate-dependent microstructures that demonstrate a mechanism for void formation due to the appearance of second-phase precipitates.

(a) Shrinkage-induced pressure

At the late stage, solidification proceeds mainly within the inter-dendritic liquid and separated eutectic liquid pools. Because of the large solid fraction in this regime, transportation of liquid is very limited. Local mass shortage due to solidification shrinkage cannot be effectively compensated by liquid transport as in traditional solidification processes. A pressure drop in the liquid appears then as the result of local mass shortage.

A basic theory in the literature that describes the above phenomenon in directional solidification is based on an effective theory that considers the mushy zone as an effective one-dimensional inter-dendritic liquid channel that terminates in a liquid reservoir. It assumes that liquid flow within the channel is driven only by a pressure gradient (Darcy's Law). The pressure drop in the liquid at distance $x=d$ from the reservoir is given by [15] $\triangle P(d)=\bar{\beta}v_n\int_0^d g(x)\,\mathrm{d}x$, where $g(x)=\mu f_l(x)/K(x)$ and where μ is the liquid viscosity, K is the mushy zone permeability and f_l is the local liquid volume fraction. The velocity of the liquid normal to the solidification front v_{ln} is given by $v_{ln}=\bar{\beta}v_n$, where v_n is the velocity of the solid–liquid front and the *shrinkage factor* $\bar{\beta}=(\rho_S-\rho_L)/\rho_L$, where ρ_S is the solid density and ρ_L is the liquid density. The boundary condition is $f_l(0)=f_l^D$, with f_l^D the upper limit of the liquid fraction where the Darcy-type flow becomes dominant. This model has been extended to incorporate elastic and plastic deformations of the solid confinement by Rappaz *et al.* [32]. The salient physics of this model involves the balance of mass flux due to liquid transport and solidification consumption. As liquid flows through microstructure with increasing solid volume fraction, a larger liquid surface area is exposed to the solidification front and more liquid mass is drawn into the solid. Meanwhile, the liquid transport becomes less effective within narrowing liquid channels, which leads to a pressure drop within the channels that cannot be fed by liquid.

The model in the previous paragraph is for pure materials and considers fluid flow. Moreover, it considers mass conservation across sharp interfaces. Nevertheless, its mechanism for pressure drop due to density change should be contained with our PFC model. As the length scale of the PFC model is limited by its atomic density resolution, we test shrinkage-induced pressure drop in a single groove geometry (figure 5) where the solid volume fraction also goes from 0 to 1, instead of a large typical mushy zone microstructure. The essential physics of mass flux balance is still retained in this simple set-up. Namely, as the PFC model uses a conserved

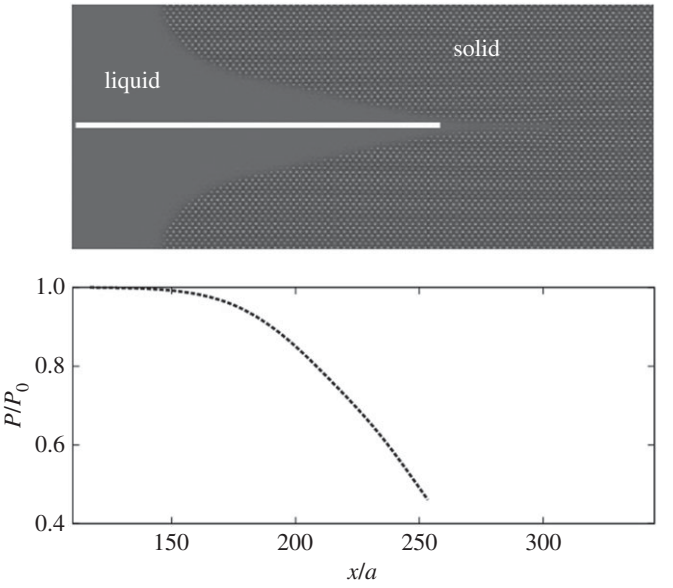

Figure 5. Pressure drop in the liquid channel due to solidification shrinkage. Local pressure is plotted along the horizontal line shown in the top figure. The '*x*'-axis is scaled with the solid lattice parameter a_1. The '*y*'-axis is scaled by the pressure far from the solidification front P_0. Pressure is measured using the standard thermodynamic relation [9]. Noise is ignored. Other model parameters are given in figure 1.

'density' field to describe the solidification, we expect that it qualitatively captures pressure drop due to solidification shrinkage. We examine the pressure drop in the test groove geometry shown in figure 5 using the PFC model formulated in equations (2.1)–(2.7) with the dynamics of equations (2.9)–(2.10). A typical pressure drop curve is shown in the bottom frame of figure 5. This resembles the same qualitative form seen in other theories. Simulations are performed in a 4096 by 512 grid box with grid spacing $\Delta x = \sqrt{3}\pi/(8q_1)$ and $\Delta y = \pi/(4q_1)$. Pressure in the liquid is measured along the centre line shown in the top frame of figure 5. As shown in the previous thermodynamics section, this model allows a low-density vapour phase to form in eutectic liquid. Thus, if the pressure drop in the liquid channel becomes large enough, it may lead to liquid cavitation. We shall examine this topic below.

(b) Solute segregation

It is well known that microsegragation of solute atoms has a strong impact on defect formation and final solidification microstructure. The SG relation has been widely used to describe microsegragation and the formation of metastable solids at high solid volume fraction [15]. To increase the solid volume fraction by $\mathrm{d}f_\mathrm{s}$, the solidification front has to reject solute $(c_\mathrm{l} - c_\mathrm{s})\mathrm{d}f_\mathrm{s}$ with $c_\mathrm{l}(c_\mathrm{s})$ the local liquid(solid) concentrations. The remaining liquid is then enriched due to this rejected solute by an amount $\mathrm{d}c_\mathrm{l} = (c_\mathrm{l} - c_\mathrm{s})\mathrm{d}f_\mathrm{s}/f_\mathrm{l}$, assuming the rejected solute atoms are evenly redistributed within the liquid. With $f_\mathrm{s} + f_\mathrm{l} = 1$, partition coefficient $k = c_\mathrm{s}/c_\mathrm{l}$ and boundary condition $c_\mathrm{l} = c_0$ at $f_\mathrm{s} = 0$, the average liquid concentration c_L can be expressed as a function of the final solid fraction f_S as

$$c_\mathrm{L} = c_0(1 - f_\mathrm{S})^{k-1}. \tag{3.1}$$

However, equation (3.1) does not take into account the effect of shrinkage-induced pressure drop that occurs in the liquid at the late stage of solidification. Specifically, since a large pressure drop may lead to gas phase nucleation in the interdendritic liquid. A crude modification of

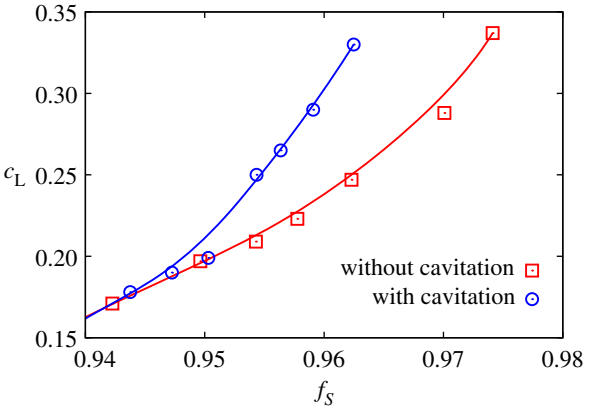

Figure 6. Solute segregation in a liquid channel at eutectic concentration with (red squares) and without (blue circles) gas phase formation in late-stage solidification. The two lines are merely a guide to the eye. The simulations start with $f_L = 0.06$, $c_L = 0.15$ and liquid density $\rho_L/\rho_S = 1.0$ for the bottom line, $\rho_L/\rho_S = 0.85$ for the top line. Cooling rate $\epsilon/t = 10^{-6}$. Solute concentration is averaged over the liquid. Noise level $2M_n/(\bar{\rho}a^d\,\mathrm{d}x\,\mathrm{d}y\sqrt{\mathrm{d}t}) = 0.03$. Other model parameters are given in figure 1. (Online version in colour.)

equation (3.1) that considers a gas phase fraction f_g can be written as

$$\int_{c_L^*}^{c_L} \frac{\mathrm{d}c_l}{c_l} = (1-k)\int_{f_S^*}^{f_S} \frac{1}{1-f_s-f_g}\,\mathrm{d}f_s, \tag{3.2}$$

where c_L^* and f_S^* are corresponding liquid concentration and solid fraction before gas phase nucleation. Because the rejected solute has to be distributed within a smaller liquid volume following gas nucleation, equation (3.2) predicts a potentially higher liquid concentration for the same solid volume fraction at the late stage of solidification. Numerical results from our PFC model qualitatively demonstrate such a behaviour in figure 6. The simulation is carried out in a quasi-one-dimensional system of 16 384 by 16 grid (one unit cell along the small dimension) where a nano-size liquid channel is enclosed by two solid slabs. To our knowledge, this is the first model that qualitatively captures this enhanced solute segregation due to gas-phase nucleation. This can lead to interesting solidification structures, as shown in the next section and Wang *et al.* [43].

(c) Solidification of liquid channel

Following the demonstration of pressure change and void formation on segregation, the PFC model is pushed a little further to examine second-phase formation in late-stage solidification of a confined inter-dendritic liquid. Instead of simulating a long inter-dendritic liquid channel, we choose to go with a solid–liquid–solid sandwich configuration which can be seen as a slab of a long channel. Starting from the top configuration in figure 7, the resulting microstructure can be vastly different depending on the cooling rate, as shown in the two middle configurations in figure 7. For the slow cooling rate, the microstructure at the end is still sandwich-like, with a stretched liquid (SL) region with enriched solute concentration similar to SG segregation. For the fast cooling rate, both gas phase (labelled as G) and β solid are observed at the end of solidification. Detailed investigation of the solidification process in this case reveals that the liquid first quickly solidifies into metastable solid precipitates, which produces a large shrinkage-induced pressure that triggers gas-phase nucleation between these precipitates. The metastable solid then decomposes to form α and β solids. Although the model is only qualitative at this point, the interplay of concentration and mass transport is shown to be an important factor in late-stage solidification.

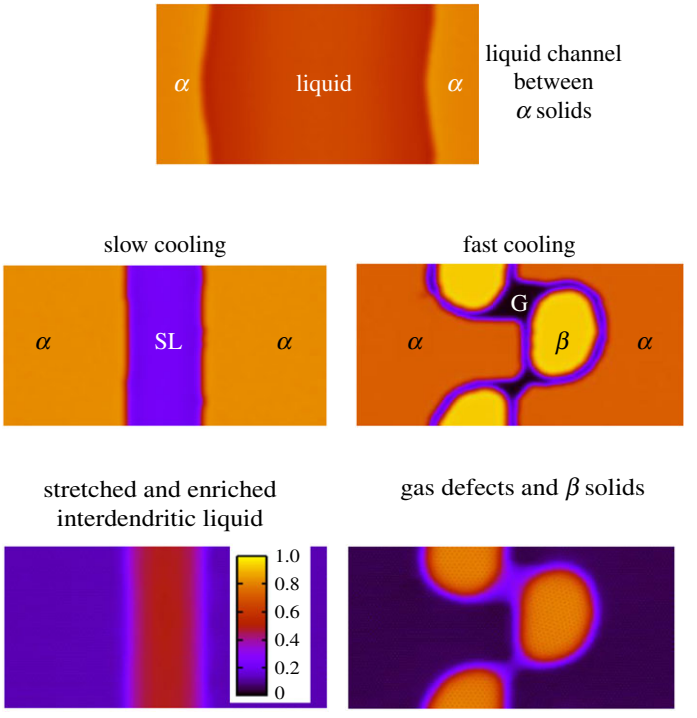

Figure 7. Solidification of inter-dendritic liquid in our PFC model. The top configuration is the starting microstructure. The middle left and bottom left are the average density and concentration maps from a slow cooling rate quench. The middle right and bottom right are the resulting average density and concentration maps from a fast cooling rate quench. Gas phase is labelled as G, SL means stretched liquid or liquid under shrinkage-induced pressure, and α and β are solid phases. The initial liquid concentration is set to 0.25 and $\rho_L/\rho_S = 0.95$. Slow cooling condition starts at $\epsilon = 0.25$ with cooling rate $\epsilon/t = 4 \times 10^{-7}$. Fast cooling condition is an instant quench to $\epsilon = 0.21$. Noise level $2M_n/(\bar{\rho}a^d\ \mathrm{d}x\ \mathrm{d}y\sqrt{\mathrm{d}t}) = 0.03$. Other model parameters are given in figure 5. The simulation is carried out in a 1024 by 512 grid with periodic boundary condition. (Online version in colour.)

4. Conclusion

A novel alloy PFC model that incorporates solid–liquid and gas-phase interactions was developed. It is the first step towards a self-consistent phase field formalism for investigating elasto-plastic effects in the late stages of rapid solidification. Here, the model is shown to qualitatively reproduce shrinkage-induced pressure drop and cavitation in inter-dendritic liquid. To our knowledge, this is the first phase field/PFC type of model that captures this important physics in solidification.

As a multiphase alloy model, it also captures an interesting microsegregation behaviour in eutectic liquid when cavitation is triggered by shrinkage-induced pressure. To our knowledge, this coupled evolution of solute concentration with shrinkage-induced pressure/cavitation in late-stage solidification has not been examined in previous experiments or theories.

Cooling rate-dependent solidification behaviours in interdendritic liquid were examined. In the case of fast cooling, the model predicted that fast solidification of eutectic liquid into metastable solids leads to void formation (which promotes solidification cracking), while the decomposition of the metastable solids leads to β and α solids. Although the parametrization of the model is only qualitative at present, the interesting phenomena it demonstrates in this work suggested that further investigation along the lines shown here may lead to new understanding of late-stage solidification processes.

The multiphase binary alloy PFC model developed in this work is also expected to be easily generalized to study the combined effect of segregation and defect nucleation in other multiphase

systems. Furthermore, its analysis using coarse-graining schemes can be used to guide the design of a complex amplitude multi-phase phase-field model for use with higher-scale simulations.

Data accessibility. No experiments were performed in this work. Numerical schemes used to obtain results are described in the main text.

Authors' contributions. N.W. and N.P. conceived of and designed the study. N.W. performed all calculations and drafted the manuscript. G.K. contributed to the idea that leads to gas phases in the PFC model. N.P. revised the manuscript. All the authors read and approved the manuscript.

Competing interests. We declare we have no competing interests.

Funding. The article is funded by National Science and Engineering Research Council of Canada, the Canada Research Chairs Program and Compute Canada.

Acknowledgements. We acknowledge Nathan Smith for helpful discussions early in this work.

Appendix A. Numerics

Implementation of the evolution equations is based on the Fourier space semi-implicit algorithm. The equation of motion for the PFC density field is relatively straightforward because the mobility parameter is assumed to be a constant. The equation for the concentration field is slightly different from the density field equation because there is a density-dependent prefactor $1+\bar{n}$, where $\bar{n}$ is a local average of n (defined in the text). Implementing of a semi-implicit algorithm for the concentration proceeds as follows: by dividing $1+\bar{n}$ on both sides of equation (2.10), the concentration equation can be rewritten as

$$\frac{\partial c}{\partial t} = \frac{M_c[\nabla(1+\bar{n})]\cdot\nabla(\delta F/\delta c)}{1+\bar{n}} + M_c\nabla\cdot\nabla\frac{\delta F}{\delta c}. \tag{A 1}$$

Retaining only the second term on the right-hand side of equation (A 1) reduces it to the standard PFC concentration dynamics which can be solved directly with the standard semi-implicit algorithm [3]. To evaluate the full equation, the 1st term on the right-hand side is first calculated in real space and then treated as a nonlinear term that is added to the second term in the standard semi-implicit algorithm for the PFC model. This approach also makes it possible to model two-sided solute diffusion in a straightforward way, although that is not considered here.

References

1. Elder KR, Grant M. 2004 Modeling elastic and plastic deformations in nonequilibrium processing using phase field crystals. *Phys. Rev. E* **70**, 051605. (doi:10.1103/PhysRevE.70.051605)
2. Elder KR, Provatas N, Berry J, Stefanovic P, Grant M. 2007 Phase-field crystal modeling and classical density functional theory of freezing. *Phys. Rev. B* **75**, 064107. (doi:10.1103/PhysRevB.75.064107)
3. Provatas N, Elder K. 2010 *Phase-field methods in material science and engineering*. Weinheim, Germany: Wiley. (doi:10.1002/9783527631520).
4. Emmerich H, Löwen H, Wittkowski R, Gruhn T, Tóth GI, Tegze G, Gránásy L. 2012 Phase-field-crystal models for condensed matter dynamics on atomic length and diffusive time scales: an overview. *Adv. Phys.* **61**, 665–743. (doi:10.1080/00018732.2012.737555)
5. Greenwood M, Provatas N, Rottler J. 2010 Free energy functionals for efficient phase field crystal modeling of structural phase transformations. *Phys. Rev. Lett.* **105**, 045702. (doi:10.1103/PhysRevLett.105.045702)
6. Wu KA, Plapp M, Voorhees PW. 2010 Controlling crystal symmetries in phase-field crystal models. *J. Phys.: Condens. Matter* **22**, 364102. (doi:10.1088/0953-8984/22/36/364102)
7. Greenwood M, Ofori-Opoku N, Rottler J, Provatas N. 2011 Modeling structural transformations in binary alloys with phase field crystals. *Phys. Rev. B* **84**, 064104. (doi:10.1103/PhysRevB.84.064104)
8. Toth GI, Tegze G, Pusztai T, Toth G, Granasy L. 2010 Polymorphism, crystal nucleation and growth in the phase-field crystal model in 2D and 3D. *J. Phys.: Condens. Matter* **22**, 364101. (doi:10.1088/0953-8984/22/36/364101)

9. Kocher G, Provatas N. 2015 New density functional approach for solid-liquid-vapor transitions in pure materials. *Phys. Rev. Lett.* **114**, 155501. (doi:10.1103/PhysRevLett.114.155501)
10. Berry J, Provatas N, Rottler J, Sinclair CW. 2014 Phase field crystal modeling as a unified atomistic approach to defect dynamics. *Phys. Rev. B* **89**, 214117. (doi:10.1103/PhysRevB.89.214117)
11. Huang ZF, Elder KR. 2009 Mesoscopic and microscopic modeling of island formation in strained film epitaxy. *Phys. Rev. Lett.* **101**, 158701. (doi:10.1103/PhysRevLett.101.158701)
12. Wu KA, Voorhees PW. 2009 Stress-induced morphological instabilities at the nanoscale examined using the phase field crystal approach. *Phys. Rev. B* **80**, 125408. (doi:10.1103/PhysRevB.80.125408)
13. Wang N, Bevan KH, Provatas N. 2016 Phase-field-crystal model for electromigration in metal interconnects. *Phys. Rev. Lett.* **117**, 155901. (doi:10.1103/PhysRevLett.117.155901)
14. Langer JS. 1980 Instability and pattern formation in crystal growth. *Rev. Mod. Phys.* **52**, 1–28. (doi:10.1103/RevModPhys.52.1)
15. Dantzig JA, Rappaz M 2009 *Solidification*. Lausanne, Switzerland: EPFL Press.
16. Boettinger WJ, Warren JA, Beckermann C, Karma A. 2002 Phase-field simulation of solidification. *Annu. Rev. Mater. Res.* **32**, 163–194. (doi:10.1146/annurev.matsci.32.101901.155803)
17. Asta M, Beckermann C, Karma A, Kurz W, Napolitano R, Plapp M, Purdy G, Rappaz M, Trivedi R. 2009 Solidification microstructures and solid-state parallels: recent developments, future directions. *Acta Mater.* **57**, 941–971. (doi:10.1016/j.actamat.2008.10.020)
18. Rappaz M, Jacot A, Boettinger WJ. 2003 Last-stage solidification of alloys: theoretical model of dendrite-arm and grain coalescence. *Metall. Mater. Trans. A* **34**, 467–479. (doi:10.1007/s11661-003-0083-3)
19. Mellenthin J, Karma A, Plapp M. 2008 Phase-field crystal study of grain-boundary premelting. *Phys. Rev. B* **78**, 184110. (doi:10.1103/PhysRevB.78.184110)
20. Wang N, Spatschek R, Karma A. 2010 Multi-phase-field analysis of short-range forces between diffuse interfaces. *Phys. Rev. E.* **81**, 051601. (doi:10.1103/PhysRevE.81.051601)
21. Rowenhorst DJ, Kuang JP, Thornton K, Voorhees PW. 2006 Three-dimensional analysis of particle coarsening in high volume fraction solid-liquid mixtures. *Acta Mater.* **54**, 2027–2039. (doi:10.1016/j.actamat.2005.12.038)
22. Souza ND, Dong HB, Ardakani GM, Shollock BA. 2005 Solidification path in the Ni-base superalloy, IN713LC—quantitative correlation of last stage solidification. *Scripta. Mater.* **53**, 729–733. (doi:10.1016/j.scriptamat.2005.05.012)
23. Heckl A, Rettig R, Cenanovic S, Göken M, Singer RF. 2010 Investigation of the final stages of solidification and eutectic phase formation in Re and Ru containing nickel-base superalloys. *J. Cryst. Growth* **312**, 2137–2144. (doi:10.1016/j.jcrysgro.2010.03.041)
24. Sistaninia M, Phillion AB, Drezet JM, Rappaz M. 2012 Three-dimensional granular model of semi-solid metallic alloys undergoing solidification: fluid flow and localization of feeding. *Acta Mater.* **60**, 3902–3911. (doi:10.1016/j.actamat.2012.03.036)
25. Montiel D, Gurevich S, Ofori-Opoku N, Provatas N. 2014 Characterization of late-stage equiaxed solidification of alloys. *Acta Mater.* **77**, 183–190. (doi:10.1016/j.actamat.2014.05.063)
26. Zhu MF, Zhang L, Zhao HL, Stefanescu DM. 2015 Modeling of microstructural evolution during divorced eutectic solidification of spheroidal graphite irons. *Acta Mater.* **84**, 413–425. (doi:10.1016/j.actamat.2014.10.057)
27. Dahle AK, Thevik HJ, Arnburg L, St. John DH. 1999 Modeling the fluid-flow-induced stress and collapse in a dendritic network. *Metall. Mater. Trans. B* **30**, 287–293. (doi:10.1007/s11663-999-0058-x)
28. Wang HF, Liu F, Yang GC. 2010 Experimental study of grain refinement mechanism in undercooled Ni–15at.%Cu alloy. *J. Mater. Res.* **25**, 1963–1974. (doi:10.1557/JMR.2010.0257)
29. Li Y, Qian D, Xue JW, Wan JC, Zhang AF, Tamura N, Song ZX, Chen K. 2015 A synchrotron study of defect and strain inhomogeneity in laser-assisted three dimensionally-printed Ni-based superalloy. *Appl. Phys. Lett.* **107**, 181902. (doi:10.1063/1.4934839)
30. Wildeman S, Sterl S, Sun C, Lohse D. 2017 Fast dynamics of water droplets freezing from the outside. *Phys. Rev. Lett.* **118**, 084101. (doi:10.1103/PhysRevLett.118.084101)

31. Niyama E, Uchida T, Morikawa M, Saito S. 1982 A method of shrinkage prediction and its application to steel casting practice. *AFS Int. Cast Met. J.* **7**, 52–63.
32. Rappaz M, Drezet JM, Gremaud M. 1999 A new hot-tearing criterion. *Metall. Mater. Trans. A* **30**, 449–455. (doi:10.1007/s11661-999-0334-z)
33. Adams JB, Wolfer WG. 1993 Void formation in rapidly-solidified metals. *Acta Metall. Mater.* **41**, 2625–2632. (doi:10.1016/0956-7151(93)90131-B)
34. Cai Y, Wu HA, Luo SN. 2014 Cavitation in a metallic liquid: homogeneous nucleation and growth of nanovoids. *J. Chem. Phys.* **140**, 214317. (doi:10.1063/1.4880960)
35. Kurz W, Trivedi R. 1991 Eutectic growth under rapid solidification conditions. *Metall. Trans. A* **22**, 3051–3057. (doi:10.1007/BF02650266)
36. Umeda T, Okane T, Kurz W. 1996 Phase selection during solidification of peritectic alloys. *Acta Mater.* **44**, 4209–4216. (doi:10.1016/S1359-6454(96)00038-9)
37. Tourret D, Gandin CA. 2009 A generalized segregation model for concurrent dendritic, peritectic and eutectic solidification. *Acta Mater.* **57**, 2066–2079. (doi:10.1016/j.actamat.2009.01.002)
38. Shuleshova O, Holland-Moritz D, Löser W, Reinhart G, Iles GN, Büchner B. 2009 Metastable formation of decagonal quasicrystals during solidification of undercooled Al-Ni melts: *in situ* observations by synchrotron radiation. *Euro. Phys. Lett.* **86**, 36002. (doi:10.1209/0295-5075/86/36002)
39. Nes E, Ryum N, Hunderi O. 1985 On the Zener drag. *Acta Metall.* **33**, 11–22. (doi:10.1016/0001-6160(85)90214-7)
40. Wang N, Wen YH, Chen LQ. 2014 Pinning force from multiple second-phase particles in grain growth. *Comput. Mater. Sci.* **93**, 81–85. (doi:10.1016/j.commatsci.2014.06.030)
41. Stefanescu DM. 2005 Computer simulation of shrinkage related defects in metal castings—a review. *Int. J. Cast Met. Res.* **18**, 129–143. (doi:10.1179/136404605225023018)
42. Asadi E, Zaeem MA. 2015 Quantifying a two-mode phase-field crystal model for BCC metals at melting point. *Comput. Mater. Sci.* **105**, 101–109. (doi:10.1016/j.commatsci.2015.03.051)
43. Wang N, Smith N, Provatas N. 2017 Investigating gas phase defect formation in late-stage solidification using a novel phase field crystal alloy model. *Phys. Rev. Mater.* **1**, 043405. (doi:10.1103/PhysRevMaterials.1.043405)